Received: 29 August 2019 | Revised: 10 April 2020 | Accepted: 18 May 2020

DOI: 10.1111/ejss.12999

ORIGINAL ARTICLE

European Journal of Soil Science WILEY

Soil pore system evaluated from gas measurements and CT images: A conceptual study using artificial, natural and 3D-printed soil cores

Mathieu Lamandé[1,2] | **Per Schjønning**[1] | **Nicola Dal Ferro**[3] | **Francesco Morari**[3]

[1]Department of Agroecology, Aarhus University, Research Centre Foulum, Tjele, Denmark

[2]Faculty of Environmental Sciences and Natural Resource Management, Norwegian University of Life Sciences, Ås, Norway

[3]Department of Agronomy, Food, Natural Resources, Animals and Environment, University of Padova, Legnaro (PD), Italy

Correspondence
Mathieu Lamandé, Department of Agroecology, Aarhus University, Research Centre Foulum, Blichers Allé 20, Postbox 50, 8830 Tjele, Denmark
Email: mathieu.lamande@agro.au.dk

Funding information
Danish Research Council for Technology and Production Sciences, Grant/Award Number: 11e106471; Seventh Framework Programme, Grant/Award Number: FP7/2007e2013; European Union Seventh Framework Programme

Abstract

Combining digital imaging, physical models and laboratory measurements is a step further towards a better understanding of the complex relationships between the soil pore system and soil functions. Eight natural 100-cm^3 soil cores were sampled in a cultivated Stagnic Luvisol from the topsoil and subsoil, which we assumed had contrasting pore systems. Artificial 100-cm^3 cores were produced from plastic or from autoclaved aerated concrete (AAC). Eight vertical holes of each diameter (1.5 and 3 mm) were drilled for the plastic cylinder and for one of the two AAC cylinders. All natural and artificial cores were scanned in an X-ray CT scanner and printed in 3D. Effective air-filled porosity, true Darcian air permeability, apparent air permeability at a pressure gradient of 5 hPa and oxygen diffusion were measured on all cores. The active pore system characteristics differed between topsoil (sponge-like, network of macropores of similar size) and subsoil (dominated by large vertical macropores). Active soil pore characteristics measured on a simplified pore network, that is, from artificial and printed soil cores, supported the fundamental differences in air transport by convection and diffusion observed between top- and subsoil. The results confirm the suitability of using the conceptual model that partitions the pore system into arterial, marginal and remote pores to describe effects of soil structure on gas transport. This study showed the high potential of using 3D-printed soil cores to reconstruct the soil macropore network for a better understanding of soil pore functions.

1 | INTRODUCTION

The fate of nutrients and pollutants, root growth of plants, soil organic matter dynamics, gas exchange and transport of water are all processes dependent on the soil pore system. A better understanding of these processes requires a good description of pore system complexity, but no single parameter can be used, and no universal method exists to describe the pore system. Numerical calculations of the processes mentioned are

useful only with a precise model for the geometry of the pore space.

Conceptual models of gas transport, such as the one by Ball (1981) or Arah and Ball (1994), need to be validated. A combination of direct (visualization) and indirect (bulk measurements) methods has shown to be useful (e.g., Obour, Schjønning, Peng, & Munkholm, 2017). Impressive developments and insights in porous media research have also been provided by X-ray micro-computed tomography (X-ray CT), which allows the microscopic visualization of the spatial arrangement of complex structures (Cnudde & Boone, 2013). However, a proper validation of conceptual models requires laboratory measurements of transport properties for perfectly described architectures closely resembling real soil pore space architecture. At the time of writing, a complete reconstruction of the soil architecture is out of reach. Soil architecture is complex because of the large range of scales at which observations and models need to apply. In addition, soil architecture is dynamic also in time. A partial reconstruction is possible today using the technique of printing in 3D. This technique is being used extensively in the industry to build complex structures. The technology has been proposed in research as a tool to integrate virtual X-ray CT information into building model materials (Behm, Waite, Hsieh, & Helmus, 2018; Matsumura, Kobayashi, Mizutani, & Bathurst, 2017; Piovesan, Achille, Ameloot, Nicolai, & Verboven, 2019; Watson et al., 2019; Zhou & Zhu, 2018). In fact, the combination of such techniques makes it possible to reconstruct complex microcosms with the heterogeneity discovered with X-ray CT, and thus to isolate the physical and chemical aspects that govern the biogeochemical and microbial processes in the soil (Ju et al., 2014; Otten et al., 2012; Ringeisen, Rincon, Fitzgerald, Fulmer, & Wu, 2015). Nowadays, with 3D printing one can replicate the diversified geometry encountered in a soil at a resolution of few micrometres. However, only a few studies have shown the potential of using 3D prints to better understand physical, mechanical or biological processes in soils (Dal Ferro & Morari, 2015; Otten et al., 2012; Ozelim & Cavalcante, 2019; Wang et al., 2017). X-ray CT imaging of 3D printed structures using different printing techniques revealed imperfections, such as clogging of parts of the pore space by printing material residues or printing-aid material, which would introduce artefacts into the physical functioning (Bacher, Schwen, & Koestel, 2015; Dal Ferro & Morari, 2015; Watson et al., 2019). In addition, as for X-ray CT imaging, the quality of the 3D printed structure depends also on the resolution of the printer in relation to the type of pore space that one tries to reconstruct.

We hypothesize that artificial pore systems and 3D prints of soil cores from X-ray CT images are useful physical models to better understand physical processes in soil. Testing this hypothesis requires the investigation of contrasting pore spaces showing fundamental differences in physical functioning. The action of the weather and the biotic community on soil structure development is most marked close to the soil surface. Therefore, a vertical gradient of soil structure is usually observed. In addition, for cultivated soils this gradient is dramatically affected by tillage. This leads to two distinctively different agricultural soil horizons in terms of quality: the topsoil and the subsoil. As mentioned by Van den Akker, Arvidsson, and Horn (2003), "The definition for the subsoil is not always clear. (...) the subsoil was defined as the soil below the cultivated layer. In this definition the panlayer is the upper part of the subsoil." This definition implies that the boundary between topsoil and subsoil will be at different depths depending on the tillage system in use (Alakukku et al., 2003). This distinction is relevant in understanding soil functioning, as large contrasts in architecture are expected between the cultivated, regularly tilled layer (the topsoil), and the mechanically undisturbed soil below (the subsoil). A regularly tilled soil layer resembles a collection of angular aggregates and clods produced through mechanical interaction with tillage tools. This leads to two main types of pore space: intra-aggregate or intra-clod space as a palimpsest of the soil pore space before tillage, and inter-aggregate or inter-clod space. The subsoil, in contrast, is characterized by the action of biota, which produce long-term or persistent, primarily vertical, macropores, and shrinkage/swelling cycles, depending on soil mineralogy. Hence, topsoils present a more sponge-like structure than subsoils, which are instead characterized by a system of macropores (arterial pores) with marginal pores branching from the macropores (Arah & Ball, 1994).

The objective of the present study was to test the potential of using artificial cores and 3D-printed specimens as soil physical models for studies of the relationships between soil structure and gas transport processes. Two contrasting natural pore systems (a regularly tilled topsoil and the subsoil beneath) were compared to simplified pore systems, from both artificial cores and 3D-printed specimens. A combination of visualization and laboratory measurements methods was used to characterize the two pore systems.

2 | MATERIALS AND METHODS

2.1 | Natural and artificial soil cores

Eight soil cores were sampled at ca. 0.08–0.12-m and ca. 0.28–0.32-m depth of a Stagnic Luvisol (four cores for each depth). Clay content was in the range

0.15–0.18 kg kg^{-1} soil. Soil organic matter was measured for the upper layer only and found to be 0.03 kg kg^{-1} soil. The soil is described in detail by Lamandé and Schjønning (2011). The sampling location was close to soils used by Naveed et al. (2016). The four cores sampled for the upper soil layer, or topsoil, were labelled S1, S2, S3 and S4, and the four for the lower soil layer, or subsoil, were labelled S5, S6, S7 and S8.

Cylinders measuring approximately 60 mm in diameter and 30 mm in height were produced from plastic or from autoclaved aerated concrete (AAC) (Figure 1). Sixteen holes of diameters 1.5 and 3 mm (eight of each) were drilled in the axial direction for the plastic cylinder, labelled "Tubes," and for one of the AAC cylinders, labelled "AAC+." The cylinder from autoclaved aerated concrete without holes was labelled "AAC−" (Figure 1).

2.2 | Acquisition of three-dimensional images

The three artificial cores were scanned with an industrial X-ray CT scanner (Phoenix v|tome|x s 240; GE Sensing and Inspection Technologies GmbH, Wunstorf, Germany), equipped with a 0.4-µm micro-focus at The Swiss Federal Institute of Technology, Zurich, with a resolution of 31.734 µm. The detector was a 16-bit 2024 × 2024 pixels. The scanner was set at a voltage of 160 kV, an exposure time of 1 s and an X-ray tube current of 190 µA. Projections were collected during a 360° sample rotation at 0.3° incremental steps. Beam hardening artefacts were minimized during data acquisition using a 0.2-mm Cu filter. The samples were scanned vertically, with a slice thickness of 31.734 µm. A total of 1,400 and 1,500 2D projections were finally reconstructed in a 16-bit greyscale depth stack for Tubes and the two AAC cores, respectively, using the Phoenix datos|x software.

The eight natural soil cores were scanned with an X-ray NIKON Metrology-CT X-Tek MCT225 scanner (Nikon Metrology, Tring, UK), equipped with a 3-µm micro-focus, under field-moist conditions at the University of Padova, with a resolution of 35.048 µm. The detector was a 16-bit 2000 × 2000 pixels and the scanner was set at a voltage of 225 kV, an exposure time of 0.5 s and an X-ray tube current of 1.0 mA. Projections were collected during a 360° sample rotation at 0.3° incremental steps. Beam hardening artefacts were minimized during data acquisition using a 0.25-mm Cu filter. The samples were scanned vertically, with a slice thickness of 35.048 µm. The acquired 1,200 2D projections were finally reconstructed in a 16-bit greyscale depth stack (ca. 855 slices of each sample) at the same resolution as for scanning using the dedicated software CT PRO 3D v. XT 3.1.9, provided by Nikon Metrology.

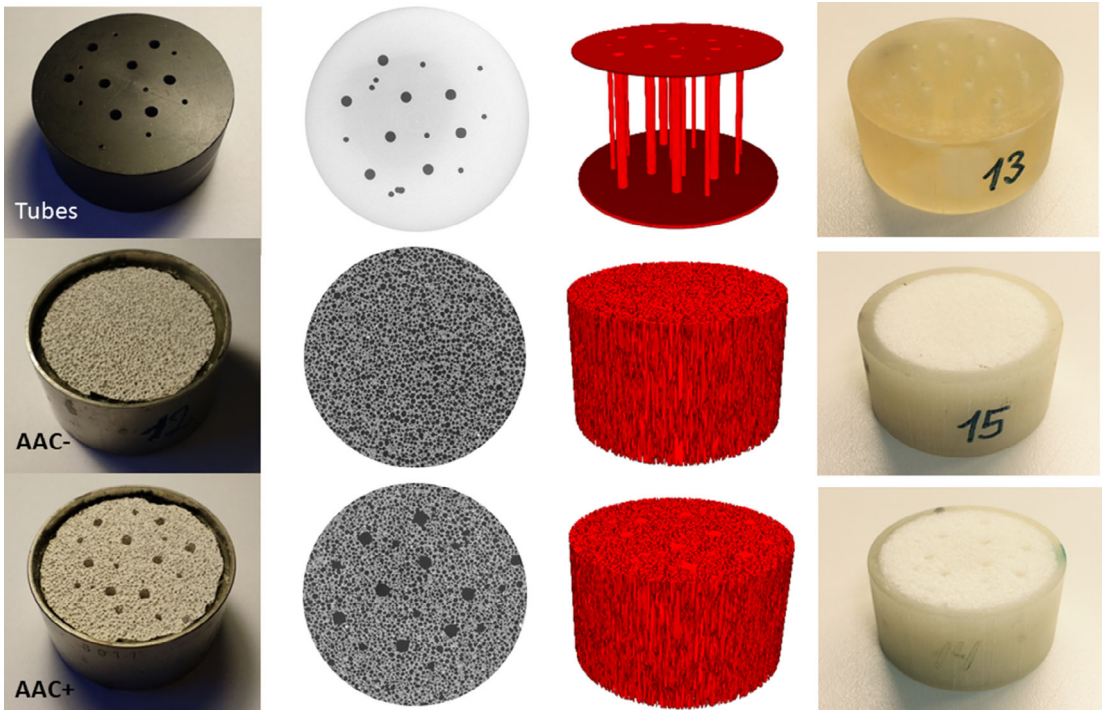

FIGURE 1 Pictures, 2D images and 3D reconstructions from X-ray computed tomography (CT) images (resolution of 31.735 µm) and 3D print of the three artificial samples: "Tubes" is a cylinder of ertacetal® C with vertical holes (1.5–3 mm); "AAC−" is a cylinder of autoclaved aerated concrete; "AAC+" is a cylinder of autoclaved aerated concrete with the same vertical holes as "tubes"

2.3 | Digital image processing

The digital image processing of greyscale reconstructed 3D stacks of each sample (both artificial and soil cores) was conducted using the public domain image processing software ImageJ (Version 1.5 k, National Institute of Health, http://rsb.info.nih.gov/ij). Greyscale 3D stacks of each artificial sample, AAC+ and AAC−, were first resized (final voxel size 63.470 μm) to simplify the image complexity that, contrarily, would have made the further 3D-modelling and 3D-printing procedure unmanageable. The original voxel size was maintained for all the other samples. After that, for each stack (both artificial and soil cores) a volume corresponding to the entire cylindrical sample was selected to exclude the sample holder (Figures 1 and 2). Every image stack was filtered with a 1-voxel 3D median filter to reduce noise. Image stacks were segmented using the 3D clustering-based threshold algorithm proposed by Otsu (1979). Only the artificial sample called "Tubes" showed some differences in greyscale intensity in the solid matrix that rendered the automatic threshold procedure unsuitable. Nevertheless, the cylindrical pores were easily visualized and consequently segmented by applying a manual threshold.

Following the procedure already proposed in Dal Ferro and Morari (2015), only percolating pores showing continuity between the top and the bottom of artificial and soil cores were selected, extracted and finally analysed with CTAn software (Version 1.12.00, Bruker micro-CT, Kontich, Belgium). As a result, the inner isolated pores (i.e., not connected to the top and the bottom) were digitally removed from the volume because they could not contribute to flow processes (e.g., gas flux) after reconstruction with 3D printing technology. Although more pore connections were likely to be present within artificial and soil cores, X-ray CT-scan imaging revealed only connections larger than resolution limits, restricting our analysis to objects larger than the CT detection capacity.

Image analysis was performed on the percolating pores and included: total porosity ($\varepsilon_{a\text{-}CT}$), as the ratio between the total number of pore voxels and total number of voxels (both labelled as pores and soil matrix); mean pore diameter (MPD), calculated according to the sphere-fitting method, where a structuring element approximates a sphere and fills every void (pore) voxel until it touches the boundary of the solid (soil) voxel (Remy & Thiel, 2002); 3D degree of anisotropy (DA), calculated according to the mean intercept length (Harrigan & Mann, 1984); and 3D Euler number (χ), an index that synthetizes the extent of pore connectivity (Vogel, Weller, & Schlüter, 2010). The χ parameter is positive when the number of isolated pores (no connections) exceeds the number of multiple connections between pores, and vice versa.

2.4 | 3D mesh generation and 3D printing

For each binarized digital volume (Tubes, AAC+, AAC−, S1 to S8), a polygonal mesh model was extracted from interconnected pore networks as in Dal Ferro and Morari (2015). The created 3D numerical models were exported to the geometric Stereo Lithographic (STL)

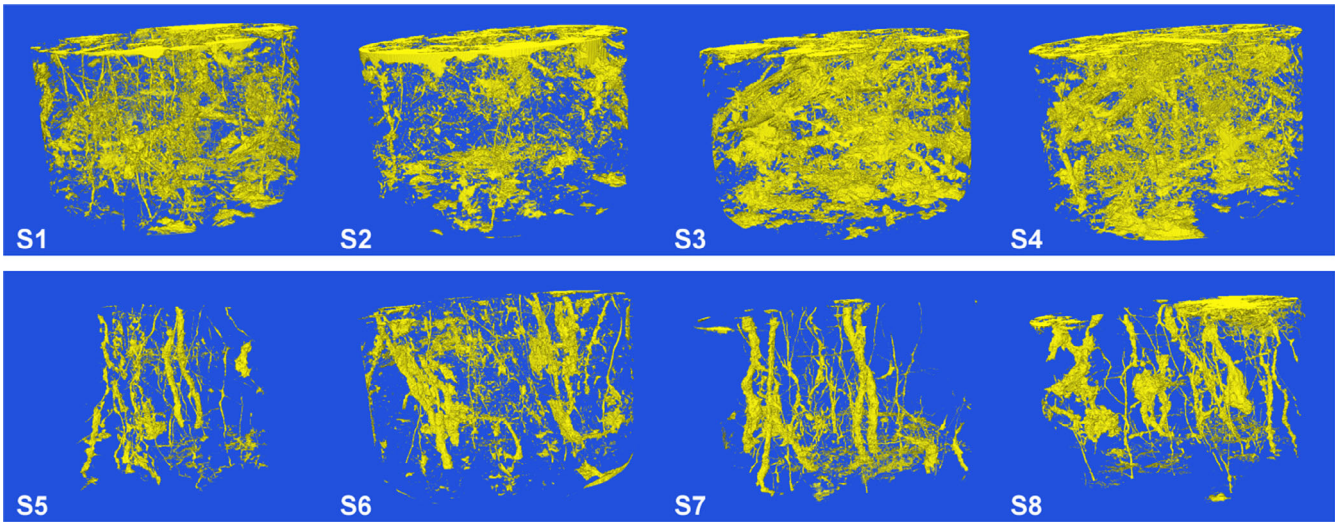

FIGURE 2 3D reconstructions from X-ray computed tomography (CT) images (resolution of 35.048 μm) of the eight soil cores from the Stagnic Luvisol (clay = 0.165 kg kg^{-1}): S1-S4 are from the topsoil (0.08–0.12 m); S5-S8 are from the subsoil (0.28–0.32 m)

format, which reproduced the surface geometry of three-dimensional pores. Each STL model was visualized with the open-source software MeshLab version 1.3.3 (Cignoni et al., 2008) to assess the continuity of pore connections along the vertical axis. An outer ring was also added to the stack edge during the 3D model reconstruction to fit the equipment for further gas diffusion and permeability analysis on the 3D-printed cores.

The 3D polygonal mesh models of all specimens were printed with a commercial ProJet 3510 HD *Plus* 3D printer (3D Systems, Inc., Rock Hill, SC, USA). The solid structure (Figures 1 and 3) was printed with resin, the exact composition of which is proprietary, but approximately contained an organic mixture of ethoxylated bisphenol A diacrylate (0.15–0.35 w/w), urethane acrylate oligomers (0.20–0.40 w/w) and tripropyleneglycol diacrylate (0.015–0.03 w/w) (Visijet Crystal, EX 200 Plastic material, Safety Data Sheet, http://www.3dsystems.com).

The 3D printer used in this study was based on multijet-printing technology: an inkjet printing deposits of either photocurable plastic resin or casting wax materials layer by layer, with a spatial resolution of 29 μm. The result was a set of 3D-printed artificial cores (composed of resin), which had pores that were filled with paraffin wax to maintain their shape during prototyping. The contact angle between water and wax, measured with a goniometer, was 120°, whereas the contact angle between pure resin and water, also measured with a goniometer, was 69°.

Wax removal was needed to empty the pores and accurately replicate the complex geometry of the samples. Ultrasonication (60 Hz) in oil at 60°C for 24 hr, followed by oven-drying at 60°C, was used for wax removal until a stabilized weight was reached (approximately 1 week) (Dal Ferro & Morari, 2015).

2.5 | Measurement procedure in the laboratory

Prior to measurements, the eight natural soil cores were capillary saturated with water on sandboxes and afterwards drained to a matric potential of −10 kPa, whereas all artificial and printed specimens were placed in a desiccator for 24 hr. The following laboratory measurements were performed for all natural, artificial and 3D-printed cores: The volume of air within the specimens in contact with the surrounding air was estimated by use of an air pycnometer and divided by the core volume to obtain the relative air-filled active pore space, $\varepsilon_{a\text{-}pyc}$ (m^3 m^{-3}). The total volume of air within the specimens was determined from the dry bulk density, the particle density, and the water content at a matric potential of −100 hPa, and divided by the core volume, ε_a (m^3 m^{-3}). The difference between ε_a and $\varepsilon_{a\text{-}pyc}$ was calculated as the blocked air-filled porosity, $\varepsilon_{a\text{-}blocked}$ (m^3 m^{-3}). The gas diffusion was measured by the one-gas, one-chamber method described by Schjønning et al. (2013), and the diffusion coefficient relative to the diffusion coefficient of

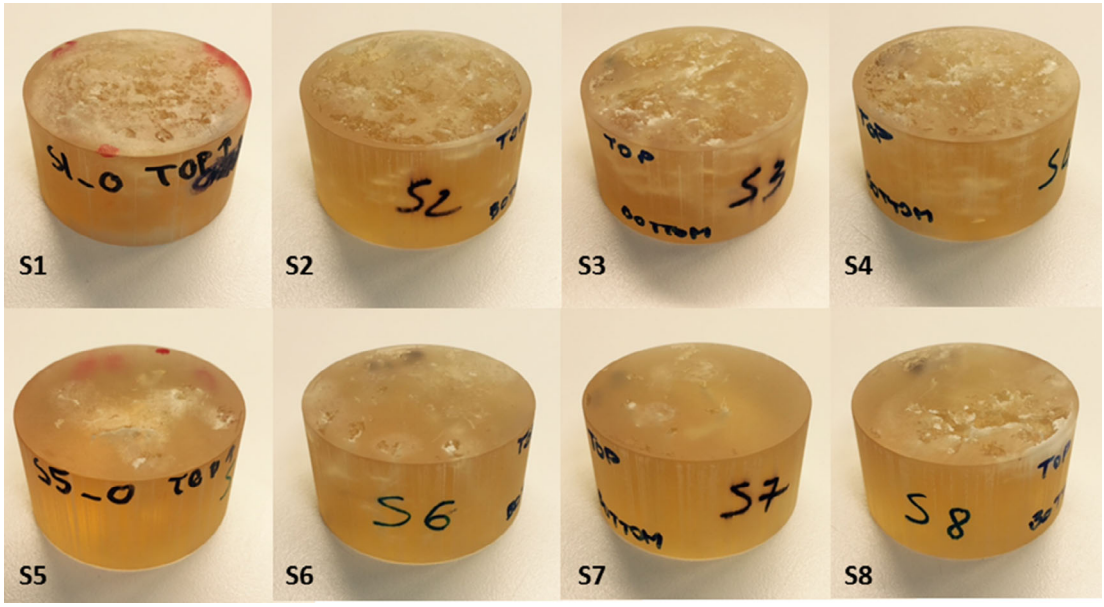

FIGURE 3 Printed natural soil cores: S1-S4 are from the topsoil (0.08–0.12 m); S5-S8 are from the subsoil (0.28–0.32 m)

oxygen in free air was determined, RD (−). In these calculations, the exact dimensions of the specific specimen were used. The air permeability was estimated by the Forchheimer approach with recently constructed equipment (Schjønning & Koppelgaard, 2017). This included measurements of airflow at four different pneumatic air pressures: 0.5, 1, 2 and 5 hPa. The true Darcy air permeability, $k_{a\text{-}Darcy}$ (μm^2), and the apparent permeability at a pneumatic pressure of 5 hPa, $k_{a\text{-}app}$ (μm^2), were estimated from the slope of the first derivative of the curve relating the superficial air velocity and the pressure gradient at a pressure difference of 0 and 5 hPa, respectively (Schjønning & Koppelgaard, 2017). The effect of viscous dissipation on air convection can be neglected due to the low viscosity of air (Raja Rani, Radhika, & Blackedge, 2017).

2.6 | Calculation of active soil pore characteristics

The relative air-filled active pore space, $\varepsilon_{a\text{-}pyc}$, the true Darcy air permeability, $k_{a\text{-}Darcy}$, and the relative diffusivity, RD, were combined to obtain the three active pore space characteristics as suggested by Ball (1981): the effective pore diameter, d_B, the tortuosity, T, and the number of pores active in air transport, n_B.

$$d_B = 2\sqrt{\frac{k_{a-Darcy}}{RD.}}, \quad (1)$$

$$T = \sqrt{\frac{\varepsilon_{a-pyc}}{RD}}, \quad (2)$$

$$n_B = \frac{{\varepsilon_{a-pyc}}^{0.5} \times RD^{1.5} \times r_s^2}{8k_{a-Darcy}}, \quad (3)$$

where r_s (m) is the sample radius.

In addition, we calculated the specific air permeability, SP, by dividing $k_{a\text{-}Darcy}$ by $\varepsilon_{a\text{-}pyc}$, as suggested by Groenevelt, Kay, and Grant (1984). Finally, for the artificial core "Tubes", we calculated the air permeability from the dimensions of the drilled holes using a combination of Darcy and Poiseuille's law, $k_{a\text{-}Poiseuille}$, as suggested by Ball (1981):

$$k_{a-Poiseuille} = \frac{\sum_{i=1}^{m} n_i r_i^4}{8r_s^2}, \quad (4)$$

where n_i is the number of holes of a given radius r_i (m) and m the number of different radii.

2.7 | Statistics

We performed a non-parametric Kruskal-Wallis test for differences between topsoil and subsoil pore system characteristics, using the R software (R Core Team, 2017).

3 | RESULTS AND DISCUSSION

3.1 | Detection of fundamental differences in air-filled pore space from laboratory measurements

The total air-filled porosity was twice as large for topsoil cores (S1-S4) than for subsoil cores (S5-S8) (Table 1), and the relative air-filled active pore space, $\varepsilon_{a\text{-}pyc}$, was nearly three times as large for topsoil cores than subsoil cores. No differences in blocked air-filled porosity could be detected between topsoils and subsoils. The Darcian air permeability, $k_{a\text{-}Darcy}$, was almost identical for topsoils and subsoils. In the topsoil, S2 had a smaller $\varepsilon_{a\text{-}pyc}$ than S1, S3 and S4. The S2 core had a very low air permeability of 0.302 μm^2. The SP of subsoil cores was roughly double that of topsoil cores according to the median values, and especially the SP for S7 was high. However, these differences were not significant ($p = .2482$). The trend indicates convective airflow in few but highly efficient air-filled pores in the subsoil, whereas a larger air-filled pore volume contributed to air transport by convection in the topsoil. The median of the RD was approximately twice as high for topsoil cores as for subsoil cores, but this difference was not significant. The topsoil S2 core displayed a very low RD value, whereas S7 had a high RD value. According to Fick's 1st law, the diffusion process is determined by the section area accessible for the gas rather than the size of the pores where gas transport occurs. These differences in RD indicate that a larger air-filled pore volume for topsoil core S2 than for subsoil core S7 contributed to air transport by diffusion.

The effective pore diameter, d_B, was generally larger for subsoils than for topsoils (Table 1). The few efficient pores expected from air transport parameters for the S7 core were reflected in the highest d_B value, whereas the many smaller efficient pores expected for S2 were reflected by the lowest d_B value. Tortuosity, T, was similar for topsoil and subsoil cores (Table 1). Interestingly, S2 had the highest value and S7 the lowest T value of all soil cores. Finally, n_B was generally higher for the topsoil than the subsoil cores, with S2 displaying the highest number of active pores (4,995) and S7 the lowest (42) (Table 1). These characteristics of the soil pores active in gas transport indicated fundamental differences in active air-filled pore space between

TABLE 1 Active soil pore characteristics measured and calculated for the topsoil and the subsoil cores

Ring no.	Specimen	ρ_b Mg m^{-3}	ε_a m^{3}m^{-3}	$\varepsilon_{a\text{-}pyc}$	$\varepsilon_{a\text{-}blocked}$	$k_{a\text{-}Darcy}$ µm^2	$k_{a\text{-}app}$ µm^2	SP µm^2	RD	d_B µm	T	n_B
S1	Topsoil	1.48	0.107	0.088	0.019	2.38	2.381	27.0	0.00471	127	4.3	4,641
S2		1.49	0.081	0.057	0.024	0.302	0.293	5.29	0.00145	81.8	6.3	4,995
S3		1.42	0.126	0.102	0.025	12.5	5.52	123	0.00415	311	4.9	781
S4		1.43	0.123	0.092	0.032	21.1	8.00	231	0.00470	379	4.4	530
Median		1.46*	0.115*	0.090*	0.024	7.5	4.0	75.2	0.00443	219	4.7	2,711
S5	Subsoil	1.77	0.044	0.022	0.022	2.21	1.42	99.1	0.00146	220	3.9	435
S6		1.70	0.056	0.033	0.023	8.39	2.94	254	0.00161	408	4.5	161
S7		1.75	0.052	0.029	0.023	96.8	17.3	3,312	0.00347	944	2.9	42
S8		1.72	0.072	0.052	0.020	4.10	3.39	79.6	0.00254	227	4.5	816
Median		1.73*	0.054*	0.031*	0.022	6.2	3.2	177	0.00208	317	4.2	298

Note: Median values marked with * were tested significantly different between topsoil and subsoil (Kruskal-Wallis test at $p < .05$).
Dry bulk density, ρ_b; total relative air-filled pore volume, ε_a; air-filled pore volume in contact with the ends of the sample, $\varepsilon_{a\text{-}pyc}$; Darcy and apparent air permeability, $k_{a\text{-}Darcy}$ and $k_{a\text{-}app}$; Normalized air permeability (values divided by $\varepsilon_{a\text{-}pyc}$), RD; effective pore diameter, d_B; tortuosity, T; number of pores per square area active in gas transport, n_B.

the topsoil (many small efficient pores) and the subsoil (few large efficient pores). The cores S2 and S7 represent the extremes for the topsoil and subsoil cores, respectively. It should be noted that, according to the capillary theory, air-filled pores of all cores should have an equivalent diameter of 30µm and above (corresponding to the matric potential −100 hPa when performing the measurements), and are therefore classified as meso- or macropores (Brewer, 1964).

3.2 | Quantification of fundamental differences in macropore space characteristics using X-ray CT imaging

According to the characterization of the visible porosity on X-ray CT images (i.e., >35 µm), topsoil cores presented a higher macroporosity, $\varepsilon_{a\text{-}CT}$, a lower Euler number, χ, and a generally larger degree of anisotropy, DA, than the subsoil cores (Table 2; *p*-values of .043, .029 and .083, respectively). Especially topsoil cores S1 and S4 seemed to have a more highly connected macroporosity than the other cores (low χ). For topsoil cores, a low χ (many redundant connections between macropores) was associated with low anisotropy (S1 and S4 vs. S2 and S3). Mean macropore diameter, MPD, was quite similar for topsoil and subsoil cores. The lower $\varepsilon_{a\text{-}CT}$ and DA, and the larger χ for the subsoil than for the topsoil cores suggest a macropore space composed of a few large macropores oriented in various directions, not connected to each other. The morphological measurements on macropores detected on X-ray CT images were in agreement with the fundamental differences in active macropores between the topsoil and the subsoil cores observed from the laboratory measurements.

TABLE 2 X-ray computed tomography (CT) parameters estimated for the topsoil and subsoil cores (median of four cores).

Specimen	$\varepsilon_{a\text{-}CT}$* m^3 m^{-3}	MPD µm	χ* Mm^{-3}	DA
Topsoil	0.037	932	−0.086	0.40
Subsoil	0.014	1,080	−0.027	0.20

Note: Medians of the parameters marked with * were significantly different between the topsoil and subsoil (Kruskal-Wallis test at $p < .05$). MPD, mean pore diameter; X, Euler number; DA, degree of anisotropy.

3.3 | Validation of the conceptual model of Ball for active air transport using artificial cores

Pore system characterization using X-ray CT images is limited by the resolution, and laboratory measurements depend on the size of the soil cores (Ozelim & Cavalcante, 2019; Piccoli, Schjønning, Lamandé, Zanini, & Morari, 2019). The effective air-filled porosity, $\varepsilon_{a\text{-}pyc}$, for the AAC material was 80% of the core volume (Table 3). The holes drilled accounted for about 2%, with the AAC+ core having a value for $\varepsilon_{a\text{-}pyc}$ of 0.82 m^3 m^{-3}. The $k_{a\text{-}Darcy}$ for AAC+ was approximately three times higher than for Tubes. This indicates that the sponge-like pore system of the concrete between the drilled holes contributed to the transport of air by convection. The $k_{a\text{-}Darcy}$ for AAC− was

dramatically lower than for the two samples with drilled holes (Tubes and ACC+). This is a strong indication that air permeability is highly dependent on the size of the pores (i.e., follows Poiseuille's law). The RD was less variable among the cores (Table 3). Theoretically, T should have values of unity for the Tubes core with straight diffusion pathways only (Ball, 1981). We observe a T value of 1.1 (Table 3). The deviation from 1 may be due to uncertainty in the dimensions of the core, which are required for the calculation of RD. However, the estimate is reasonably close to 1, which confirms that the diffusion is simply determined by the square area available for the diffusion process. The larger deviation from unity of T for the other specimens is an indication of the presence of sponge-like pores connected to the drilled holes (Tables 1 and 3). Assuming a Darcian flow of air, the gas movement in Tubes should be the sum of the contributions of the 16 paths (Ball, Harris, & Bruford, 1981). Therefore, d_B (1.68 mm; Table 2) would represent an estimate of the average diameter of the drilled holes. An average of 2.25 mm was calculated on the physical core from the size of the drill. Hence, we note that Ball's model estimated a lower d_B for "Tubes". This may be related to turbulences in the largest pores (diameter of 3 mm).

Schjønning (2019) reported that Ball's d_B calculation using RD and $k_{a\text{-Darcy}}$ was accurate for tubular pores of 1 and 2 mm diameter, but was not able to estimate the diameter for tubular pores of 4.5 and 5.8 mm. For such large pores, the average pore air velocity becomes too large to retain a Darcian flow, thus disqualifying even the Forchheimer methodology for estimation of $k_{a\text{-Darcy}}$ (Schjønning, 2019). This means that, for Tubes, the too low d_B as compared to the physical core relates to an underestimation of $k_{a\text{-Darcy}}$ due to non-Darcian flow. Based on the tortuosity close to unity, we can assume a correct estimation of $\varepsilon_{a\text{-pyc}}$ and RD for Tubes and a $k_{a\text{-Darcy}}$ value of 3,583 μm^2 would therefore correspond to a d_B of 2.25 mm (Equation 1). Air permeability calculated from the dimensions of the drilled holes of Tubes using a combination of Darcy and Poiseuille's law as suggested by Ball (1981) was $k_{a\text{-Poiseuille}} = 5{,}355\ \mu m^2$ (Equation 4). Revisiting $k_{a\text{-Darcy}}$ measurements for tubular pores of various diameters from Schjønning (2019), we observed a good agreement between $k_{a\text{-Darcy}}$ and $k_{a\text{-Poiseuille}}$ for tubular pores up to 2 mm in diameter, and a lower $k_{a\text{-Darcy}}$ than $k_{a\text{-Poiseuille}}$ for tubular pores with larger diameters (Figure 4). This supports the above theory: (a) that there was an underestimation of $k_{a\text{-Darcy}}$ for Tubes, probably because of turbulences in the 3-mm holes; and (b) that the contribution of each tubular hole of Tubes could be added to approximate $k_{a\text{-Poiseuille}}$ (Equation 4). As expected, the d_B-estimate of the AAC+ core was larger than for AAC− due to the drilled holes. The sponge-like pores of the AAC+ material thus affected the "effective" diameter in both diffusion and convection processes, also confirmed by the low d_B values for the AAC− core. T was higher for the AAC− specimen than for the AAC+ specimens, as expected. We observed n_B values of 35 for the Tubes core when 16 holes were drilled. This value was larger than expected, although of the correct magnitude. The overestimation of n_B is probably related to the underestimation of $k_{a\text{-Darcy}}$, as discussed earlier. In contrast, we have much higher n_B values for the AAC cores than for Tubes. The higher n_B value for AAC− than for AAC+ indicates, again, that sponge-like pores contributed to air transport through this material, and that the presence of a few additional large macropores modified drastically the mode of air transport through the core.

The Tubes represent a soil structure composed of a water-saturated matrix with a few large continuous macropores (root channels, earthworm burrows, cracks). The AAC cores showed an air-filled macroporous matrix, and both $k_{a\text{-Darcy}}$ and RD were several orders of magnitude larger than for real soils. However, after normalization by the effective air-filled porosity, the S7 subsoil core showed SP and T values between those for AAC+ and AAC− (Tables 1 and 4). This confirms that the efficient pore system at −10 kPa matric potential for S7 included some large air-filled continuous pores. Using the three active soil pore characteristics, d_B, T and n_B as defined by Ball (1981), we were able to detect the few large macropores that differentiated AAC+ from AAC−, which represented only 2% of the efficient porosity, confirming the differences identified between topsoil and subsoil cores.

TABLE 3 Active soil pore characteristics measured and calculated for the artificial cores

Specimen	$\varepsilon_{a\text{-pyc}}$ m^3m^{-3}	$k_{a\text{-Darcy}}$ μm^2	$k_{a\text{-app}}$ μm^2	SP μm^2	RD	d_B μm	T	n_B
Tubes	0.0271	2005	448	73,752	0.0227	1,683	1.1	35
AAC+	0.8202	5,905	705	7,199	0.1169	1,272	2.6	941
AAC−	0.8012	25.7	14.9	32.0	0.0895	95.8	3.0	93,978

Autoclaved aerated concrete, AAC; Air-filled pore volume in contact with the ends of the sample, $\varepsilon_{a\text{-pyc}}$; Darcy and apparent air permeability, $k_{a\text{-Darcy}}$ and $k_{a\text{-app}}$; Normalized air permeability (values divided by $\varepsilon_{a\text{-pyc}}$), relative diffusivity, RD; effective pore diameter, d_B; tortuosity, T; number of pores per square area active in gas transport, n_B.

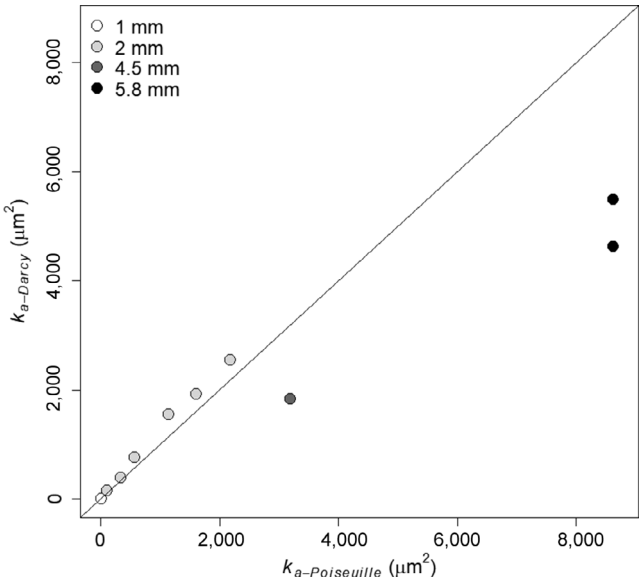

FIGURE 4 Air permeability calculated from the dimensions of the drilled holes of tubes using Poiseuille's law, $k_{a\text{-}Poiseuille}$, as suggested by Ball et al. (1981) (Equation (4)) against the Darcian air permeability measurements for tubular pores of various diameters, $k_{a\text{-}Darcy}$, from Schjønning (2019)

TABLE 4 X-ray computed tomography (CT) parameters estimated for the artificial cores

Specimen	$\varepsilon_{a\text{-}CT}$ m^3 m^{-3}	MPD µm	χ mm^{-3}	DA
Tubes	0.023	2,652	0.0002	0.86
AAC+	0.518	888	−3.94	0.19
AAC−	0.464	775	−1.31	0.13

AAC, autoclaved aerated concrete; MPD, mean pore diameter; X, Euler number; DA, degree of anisotropy.

3.4 | Using 3D-printed soil cores to explore the effects of soil pore characteristics on air transport

Combinations of physical measurements on soil cores in the laboratory helped identify some morphological characteristics of the air-filled pore space of naturally structured soil cores (Table 1). The use of very simple physical models (Tubes, ACC− and ACC+) confirmed the assumptions of differences between topsoil and subsoil morphology of the air-filled pore space derived from the active soil pore characteristics (see discussion in the previous sub-section). The next step was to investigate the physical functioning of a well-defined architecture that was more complex than the three simple models, but not as complex as the natural soil cores. We chose to use 3D prints of the part of the pore network participating in air transport through the cores that was visible on the X-ray

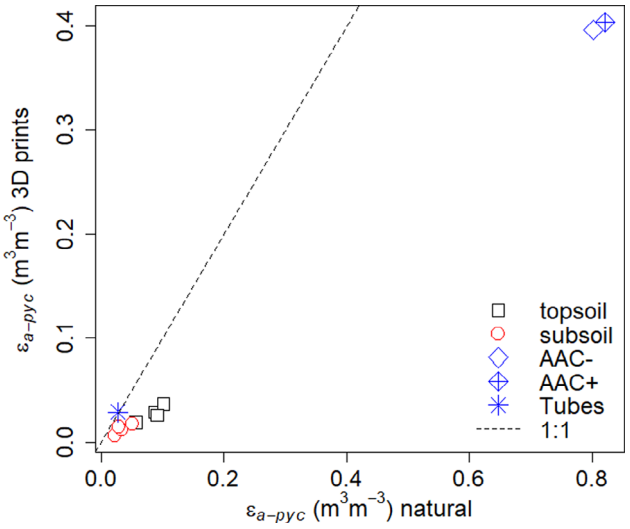

FIGURE 5 Effective air-filled porosity, $\varepsilon_{a\text{-}pyc}$, for natural and artificial cores and their 3D-printed counterpart

CT images and connected to both ends of the core faces. In that way, the physical model Tubes and its printed counterpart should be identical, apart from the pore wall surface properties of the two materials (Figure 1). Effectively, only small differences in active soil pore characteristics were observed between Tubes and its printed counterpart 3D Tubes (Figure 5; Tables 3 and 5). As expected, for all other natural and artificial cores, the printed counterpart presented a lower $\varepsilon_{a\text{-}pyc}$, meaning that the printing excluded some pores (Figure 5). Note that $\varepsilon_{a\text{-}pyc}$ was less reduced by printing for the subsoil cores than for the topsoil cores (a reduction of 58% and 69%, respectively). The $k_{a\text{-}Darcy}$ was too low to be measured for the printed specimen of topsoil core S2 (Table 5). SP was larger for the printed than for the real cores for S3, S4, S5, S6 and S7 (Tables 1 and 5). This was expected for all cores, as only the pores connected from top to bottom of the cores were printed. However, S1 (topsoil) and S8 (subsoil) showed a larger SP for the real cores than for the 3D-printed cores. SP was very large for printed S5, S6 and S7 subsoil cores. The printed S7 core showed an SP similar to AAC+ (7,618 µm^2 and 7,199 µm^2, respectively). For all topsoil and subsoil printed cores, RD was lower than for the real samples (Tables 1 and 5). These results were also expected, as a large part of the air-filled pore system was not detectable on X-ray CT images and hence in the 3D-printed specimens. For all cores but S1 and S8, d_B was larger for the printed than for the real cores. This confirms that if present (i.e., not for S8), large air-filled macropores control gas transport in soil. Notice the much larger d_B for the printed version of the S4 (topsoil) than for the real soil core. This indicates that many pores smaller than 29 µm were effective for the real soil cores. Tortuosity was similar for real and printed cores for the three artificial

TABLE 5 Active soil pore characteristics measured and calculated for the 3D-printed version of the natural soil cores and artificial cores

Ring no.	Specimen	$\varepsilon_{a\text{-}pyc}$ m^3m^{-3}	$k_{a\text{-}Darcy}$ μm^2	$k_{a\text{-}app}$ μm^2	SP μm^2	RD -	d_B µm	T -	n_B -
S1	Topsoil	0.029	0.254	0.155	9.28	0.00128	70.7	4.6	3,496
S2		0.019	Nd	Nd	Nd	0.00140	Nd	3.6	Nd
S3		0.037	8.85	1.85	234	0.00123	480	5.5	107
S4		0.026	106	4.67	3,828	0.00124	1,660	4.7	8
Median		0.027*	8.85	1.85	234	0.00126*	480	4.7*	107
S5	Subsoil	0.006	3.51	0.620	825	0.00161	264	1.6	164
S6		0.012	14.7	2.53	1,524	0.00174	520	2.4	61
S7		0.015	118	14.87	7,618	0.00393	982	2.0	29
S8		0.017	0.433	0.236	27.5	0.00149	96.6	3.3	2005
Median		0.013*	9.08	1.58	1,175	0.00167*	392	2.2*	112
Tubes		0.0290	1989	444	68,617	0.03168	1,677	1.1	37
AAC+		0.4033	4,763	707	11,810	0.05814	1,619	2.6	183
AAC−		0.3961	59.3	32.4	150	0.02266	245	3.5	5,536

Note: Median values marked with * were significantly different between the topsoil and subsoil (Kruskal-Wallis test at $p < .05$).
Autoclaved aerated concrete, AAC; air-filled pore volume in contact with the ends of the sample, $\varepsilon_{a\text{-}pyc}$; Darcy and apparent air permeability, $k_{a\text{-}Darcy}$ and $k_{a\text{-}app}$; Normalized air permeability (values divided by $\varepsilon_{a\text{-}pyc}$), RD; effective pore diameter, d_B; tortuosity, T; number of pores per square area active in gas transport, n_B

specimens and for three out of four topsoil cores (Tables 1 and 5). In contrast, T was smaller for all printed subsoil cores than for their natural counterpart. This indicates that marginal air-filled pores were removed in the printed version of the natural subsoil cores. Tortuosity was smaller for subsoil than for topsoil printed cores. This also supports the suggestion of an active pore system dominated by large macropores for the subsoil.

Only very small pressure gradients ensure that inertial forces are kept low during air permeability measurements. Increasing the pressure gradient for measuring air permeability will move the air flow away from a Darcian flow regime (i.e., away from a linear relationship between pressure gradient and flow rate). An increase of the inertial forces will reduce the air flow velocity and consequently the air permeability. For a given increase in pressure gradient, the level of inertial forces will be related to the morphology of the active air-filled pore space (Schjønning et al., 2013; Schjønning, Pulido-Moncada, Munkholm, & Iversen, 2019). Surface roughness, but also the amount of convolution of the air-filled pore space may induce larger differences in acceleration during the flow. Figure 6 presents the ratio, R_S, of $k_{a\text{-}app}$ to $k_{a\text{-}Darcy}$, for all natural specimens and their 3D-printed counterparts. For the three artificial cores, R_S values were similar for the real cores and their printed counterparts, indicating that the 3D prints from the 63-µm resolution images were good proxies for these materials. It also indicates that only very few pores smaller than 63 µm participated significantly in convective air flow for the two AAC cores. For AAC+, there is a dominant contribution of the drilled holes to convective air flow. For AAC−, there was a noticeable number of continuous macropores larger than 63 µm, as also supported by the MPD being larger than 775 µm (Table 3). Similar R_S values for Tubes and its printed counterpart indicate a similar air friction on the surface of the two materials. In contrast, all printed versions showed a lower R_S to different degrees than the real cores. This means there is an increase in the inertial forces during convective flow through the printed cores with an increase in the pressure gradient. The printed pore system is a simplification of the real pore system for all specimens, which means a reduction of roughness and convolutions and a move toward a pore system dominated by arterial pores. The active pore space of the natural S7 specimen was dominated by large (arterial) pores, which were detectable on X-ray CT images and hence printed. S7 was close to the 1:1 line, like the artificial specimens. In contrast, the elimination of part of the marginal pores induced a large decrease in R_S for S1.

As shown by Schjønning (2019), an increase in air velocity is related to an increase in turbulence during the flow. For all soil cores but S1 and S8, the printing led to an increase in average air pore velocity and a decrease of R_S (Figure 7). The increase of inertial forces during convective flow through the printed cores is then

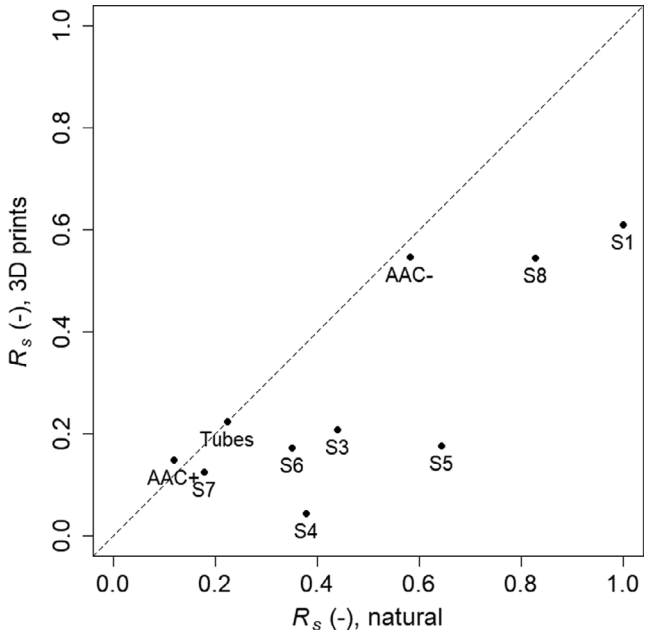

FIGURE 6 Ratio of the apparent air permeability measured at 5 hPa pressure gradient to Darcy air permeability ($R_s = k_{a\text{-}app}/k_{a\text{-}Darcy}$) for natural and artificial cores against the same ratio for the corresponding 3D-printed cores

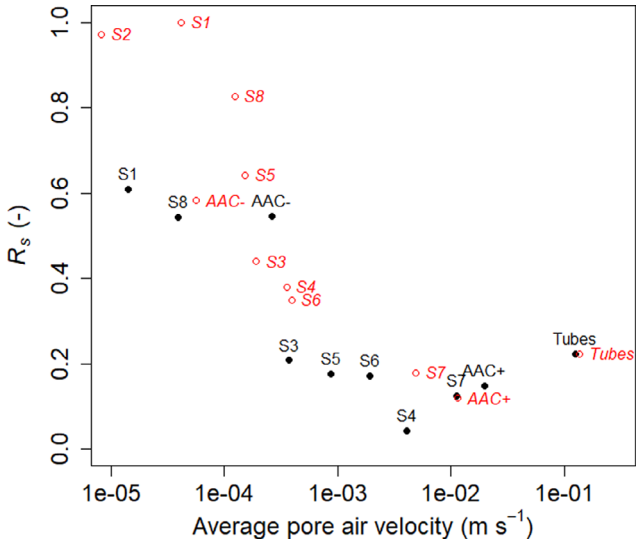

FIGURE 7 Ratio of the apparent air permeability measured at 5 hPa pressure gradient to Darcy air permeability ($R_s = k_{a\text{-}app}/k_{a\text{-}Darcy}$) against the average pore air velocity (m s^{-1}) for natural and artificial cores (in red and italics) and their 3D-printed counterparts (in black). Please note the log-scale for the average pore air velocity

related to an increase in average air pore velocity. This is in accordance with previous observations (Schjønning et al., 2019; Schjønning & Koppelgaard, 2017). Only two cores, S1 and S8, showed a decrease in average pore air velocity with a decrease of R_S when printed (Figure 7). Interestingly, S1 and S8 were the only two cores showing a larger SP for the natural than for the printed specimens. For these two cores, $k_{a\text{-}Darcy}$ for the printed specimens was very low (<1 μm^2). This can be explained by printing inaccuracy and clogging of pores by the wax used to fill the pore space during printing (Dal Ferro & Morari, 2015). Bacher et al. (2015), Dal Ferro and Morari (2015) and Watson et al. (2019) observed, using X-ray CT imaging of the printed specimens, inaccuracy of the 3D printing techniques, either during printing or the removing of materials used to fill the pore space during printing. Particularly for the printing technique used in our study, full wax removal in small pores of complex structures can be difficult to achieve, even after ultrasonication in oil and oven-drying (Dal Ferro & Morari, 2015). The smallest difference in R_S was observed between S7 and its printed counterpart (0.18 and 0.13, respectively), indicating that the macropore system conducting most of the air flow through this core was similar for the real and the printed cores (Figure 6). The largest difference in R_S for subsoil cores was observed between S5 and its printed counterpart (0.64 and 0.18, respectively). For S5, a large number of air-filled pores must have been active for the real core but not for the printed one, and the high velocity of air flow through the remaining macropores with a pressure gradient of 5 hPa might explain the decrease in R_S. The largest difference in R_S for topsoil cores was observed for S1 and its printed counterpart (1.00 and 0.61, respectively). Generally, these results showed the potential of using 3D prints to better understand physical processes in soils related to air transport, as also suggested by Bacher et al. (2015), Dal Ferro and Morari (2015) and Ozelim and Cavalcante (2019) for physical processes related to water transport.

4 | CONCLUSIONS

We were able to reveal in detail fundamental differences in the air-filled macropore system between a regularly tilled layer (topsoil) and the mechanically undisturbed layer below (subsoil) using a combination of laboratory measurements and X-ray CT imaging on natural, artificial and 3D-printed specimens. As expected, the pore system for subsoil was dominated by large continuous macropores, and the topsoil was characterized by a dense network of smaller macropores. In addition, the use of the three types of specimens helped the evaluation of the conceptual model of active pore space based on air transport parameters proposed by Ball (1981). Printed versions of cores were good proxies for natural samples for specimens where air-filled pore space was dominated by large continuous macropores. Analysis of the recently developed functional parameter, the air permeability ratio, for

the natural and artificial cores, and their printed counterparts, indicated that Darcian and apparent air permeability measurements are powerful tools for detecting fundamental differences in pore space morphology. Improvements in digital imaging and 3D print technologies will allow broadening of the investigation of gas transport at the micropore scale.

ACKNOWLEDGEMENTS

The technical assistance of S.T. Rasmussen and M. Naveed with sampling in the field, and of B.B. Christensen and M. Koppelgaard with laboratory measurements is gratefully acknowledged. We thank T. Keller for facilitating the X-ray CT scanning of the three artificial cores used in this study, and M. Naveed for his help in producing Figure 1. This work was funded partly by the RECARE project, receiving funding from the European Union Seventh Framework Programme (FP7/2007e2013) under grant agreement no. 603498, and partly by the "StressSoil" project by the Danish Research Council for Technology and Production Sciences (Project No. 11e106471).

CONFLICT OF INTEREST

None

ORCID

Mathieu Lamandé https://orcid.org/0000-0003-4211-9395

Nicola Dal Ferro https://orcid.org/0000-0001-7957-3212

REFERENCES

Alakukku, L., Weisskopf, P., Chamen, W. C. T., Tijink, F. G. J., van der Linden, J. P., Pires, S., ... Spoor, G. (2003). Prevention strategies for field traffic-induced subsoil compaction: A review: Part 1. *Machine/Soil Interactions. Soil & Tillage Research*, *73*, 145–160.

Arah, J. R. M., & Ball, B. C. (1994). A functional model of soil porosity used to interpret measurements of gas diffusion. *European Journal of Soil Science*, *45*, 135–144.

Bacher, M., Schwen, A., & Koestel, J. (2015). Three-dimensional printing of macropore networks of an undisturbed soil sample. *Vadose Zone Journal*, *14*. https://doi.org/10.2136/vzj2014.08.0111

Ball, B. C. (1981). Modelling of soil pores as tubes using gas permeabilities, gas diffusivities and water release. *Journal of Soil Science*, *32*, 465–481.

Ball, B. C., Harris, W., & Bruford, J. R. (1981). A laboratory method to measure gas diffusion and flow in soil and other porous materials. *Journal of Soil Science*, *32*, 323–333.

Behm, J., Waite, B. R., Hsieh, S. T., & Helmus, M. R. (2018). Benefits and limitations of three-dimensional printing technology for ecological research. *BMC Ecology*, *18*, 32.

Brewer, R. (1964). *Fabric and mineral analysis of soils* (p. Click here to enter text.). New York: Wiley.

Cignoni, P., Callieri, M., Corsini, M., Dellepiane, M., Ganovelli, F., & Ranzuglia, G. (2008). Meshlab: An open-source mesh processing tool. In Proceedings: 6th Eurographics Italian Chapter Conference (pp. 129-136). Salerno, Italy.

Cnudde, V., & Boone, M. N. (2013). High-resolution X-ray computed tomography in geosciences: A review of the current technology and applications. *Earth-Science Reviews*, *123*, 1–17.

Dal Ferro, N., & Morari, F. (2015). From real soils to 3D-printed soils: Reproduction of complex pore network at the real size in a silty-loam soil. *Soil Science Society of America Journal*, *79*, 1008–1017.

Groenevelt, P. H., Kay, B. D., & Grant, C. D. (1984). Physical assessment of a soil with respect to rooting potential. *Geoderma*, *34*, 101–114.

Harrigan, T. P., & Mann, R. W. (1984). Characterization of microstructural anisotropy in orthotropic materials using a second rank tensor. *Journal of Materials Science*, *19*, 761–767.

Ju, Y., Xie, H., Zheng, Z., Lu, J., Mao, L., Gao, F., & Peng, R. (2014). Visualization of the complex structure and stress field inside rock by means of 3D printing technology. *Chinese Science Bulletin*, *59*, 5354–5365.

Lamandé, M., & Schjønning, P. (2011). Transmission of vertical stress in a real soil profile. Part I: Site description, evaluation of the Söhne model, and the effect of topsoil tillage. *Soil & Tillage Research*, *114*, 57–70.

Matsumura, S., Kobayashi, T., Mizutani, T., & Bathurst, R. J. (2017). Manufacture of bonded granular soil using X-ray CT scanning and 3D printing. *Geotechnical Testing Journal*, *40*(6), 1000–1010.

Naveed, M., Schjønning, P., Keller, T., de Jonge, L. W., Moldrup, P., & Lamandé, M. (2016). Quantifying vertical stress transmission and compaction-induced soil structure using sensor mat and X-ray computed tomography. *Soil & Tillage Research*, *158*, 110–122.

Obour, P. B., Schjønning, P., Peng, Y., & Munkholm, L. J. (2017). Subsoil compaction assessed by visual evaluation and laboratory methods. *Soil & Tillage Research*, *173*, 4–14.

Otsu, N. (1979). A threshold selection method from gray-level histograms. *IEEE Transactions on Systems, Man, and Cybernetics*, *9*, 62–66.

Otten, W., Pajor, R., Schmidt, S., Baveye, P. C., Hague, R., & Falconer, R. E. (2012). Combining X-ray CT and 3D printing technology to produce microcosms with replicable, complex pore geometries. *Soil Biology and Biochemistry*, *51*, 53–55.

Ozelim, L. C. d. S. M., & Cavalcante, A. L. B. (2019). Combining microtomography, 3D printing, and numerical simulations to study scale effects on the permeability of porous media. *International Journal of Geomechanics*, *19*, 04018194.

Piccoli, I., Schjønning, P., Lamandé, M., Zanini, F., & Morari, F. (2019). Coupling gas transport measurements and X-ray tomography scans for multiscale analysis in silty soils. *Geoderma*, *338*, 576–584.

Piovesan, A., Achille, C., Ameloot, R., Nicolai, B., & Verboven, P. (2019). Pore network model for permeability characterization of three-dimensionally-printed porous materials for passive microfluidics. *Physical Review E*, *99*, 033107.

R Core Team. (2017). R: A Language and Environment for Statistical Computing. Retrieved from https://www.R-project.org/.

Raja Rani, T., Radhika, T. S. L., & Blackedge, J. M. (2017). The effect of viscous dissipation on convection in a porous medium. *Mathematica Aeterna*, *7*, 131–145.

Remy, É., & Thiel, É. (2002). Medial axis for chamfer distances: Computing look-up tables and neighbourhoods in 2D or 3D. *Pattern Recognition Letters*, *23*, 649–661.

Ringeisen, B. R., Rincon, K., Fitzgerald, L. A., Fulmer, P. A., & Wu, P. K. (2015). Printing soil: A single-step, high-throughput method to isolate micro-organisms and near-neighbour microbial consortia from a complex environmental sample. *Methods in Ecology and Evolution*, *6*, 209–217.

Schjønning, P. (2019). A note on the Forchheimer approach for estimating soil air permeability. *Soil Science Society of America Journal*, *83*, 1067–1072. https://doi.org/10.2136/sssaj2018.12.0484

Schjønning, P., & Koppelgaard, M. (2017). The Forchheimer approach for soil air permeability measurement. *Soil Science Society of America Journal*, *81*, 1045–1053.

Schjønning, P., Lamandé, M., Berisso, F. E., Simojoki, A., Alakukku, L., & Andreasen, R. R. (2013). Gas diffusion, non-Darcy air permeability and CT images of a clay subsoil affected by compaction. *Soil Science Society of America Journal*, *77*, 1977–1990.

Schjønning, P., Pulido-Moncada, M., Munkholm, L. J., & Iversen, B. V. (2019). Ratio of non-darcian to darcian air permeability as a marker of soil pore organisation. *Soil Science Society of America Journal*, *83*, 1024–1031. https://doi.org/10.2136/sssaj2018.11.0452

Van den Akker, J. J. H., Arvidsson, J., & Horn, R. (2003). Introduction to the special issue on experiences with the impact and prevention of subsoil compaction in the European Union. *Soil Tillage Research*, *73*, 1–8.

Vogel, H. J., Weller, U., & Schlüter, S. (2010). Quantification of soil structure based on Minkowski functions. *Computers & Geosciences*, *36*, 1236–1245.

Wang, L., Ju, Y., Xie, H., Ma, G., Mao, L., & Hue, K. (2017). The mechanical and photoelastic properties of 3D printable stress-visualized materials. Scientific Reports 7, paper no 10918.

Watson, F., Maes, J., Geiger, S., Mackay, E., Singleton, M., McGravie, T., ... Hasiuk, F. (2019). Comparison of flow and transport experiments on 3D printed micromodels with direct numerical simulations. *Transport in Porous Media*, *129*, 449–466.

Zhou, T., & Zhu, J. B. (2018). Identification of a suitable 3D printing material for mimicking brittle and hard rocks and its brittleness enhancements. *Rock Mechanics and Rock Engineering*, *51*, 765–777.

How to cite this article: Lamandé M, Schjønning P, Dal Ferro N, Morari F. Soil pore system evaluated from gas measurements and CT images: A conceptual study using artificial, natural and 3D-printed soil cores. *Eur J Soil Sci*. 2020;1–13. https://doi.org/10.1111/ejss.12999